LA-UR- 09-01174

Approved for public release;
distribution is unlimited.

Title:	Development and Validation of a Two-Dimensional Fast-Response Flood Estimation Model
Author(s):	David Judi Steven Burian Timothy McPherson
Intended for:	Journal of Flood Risk Management

Los Alamos
NATIONAL LABORATORY
EST. 1943

Form 836 (7/06)

CHAPTER 2

DEVELOPMENT AND VALIDATION OF A TWO-DIMENSIONAL FAST-RESPONSE FLOOD ESTIMATION MODEL

2.1 Introduction

On average, each year about 196 million people in more than 90 countries are exposed to catastrophic flooding, resulting in more than 170,000 deaths (UNDP 2004). In the United States, flooding is the leading cause of disaster, accounting of nearly two-thirds of all federal disasters and causing approximately $50 billion in property damage in the 1990s (Downton et al. 2005). Tropical Storm Allison in June, 2001 was one of the most damaging tropical storms, spanning thousands of square kilometers across Texas, Louisiana, and Eastern United States, with losses exceeding $5 billion (Service Assessment Report 2001). Although flood losses tend to fluctuate from year to year, there has been an increasing trend over the past century (Pielke and Downtown 2000), which has been attributed to both change in climate as well as population growth and development in flood-prone regions (Pielke et al. 2002).

To mitigate the impacts of flooding, the United States instituted the National Flood Insurance Program (NFIP) to reduce flood damage and costs associated with disaster assistance (FEMA 2006). The program aims to accomplish this with floodplain identification and mapping, establishing guidelines and recommendations for floodplain

management, and requiring flood insurance for property located within the identified floodplain. Although the floodplain maps generated through the program were created for insurance and floodplain management purposes, it has been found that these maps are now used for many other purposes, including disaster mitigation, land-use planning, and emergency response (NRC 2009). There are many inherent problems when using these maps developed for flood insurance purposes for planning and emergency response, as well as consequence assessment. First, the maps don't exist for all locations, and the maps that do exist may be obsolete. This is because maps have only been developed for approximately 1 million miles of the Nations 3.5 million miles of river and coast (NRC 2009), and about 75% of the NFIP flood maps Nationwide are more than 10 years old (FEMA, 2002) and, therefore, do not accurately represent changing hydrological and environmental features (NRC 2009). As an example, a post-disaster study of Tropical Storm Allison, which was estimated at near a 500-year storm event, revealed that of the approximately 45,000 flooded buildings, only 7,000 were actually located within the 100-year floodplain identified by NFIP flood risk maps (Sinnock 2001).

The second key limitation of using NFIP flood maps in emergency response and disaster mitigation is that they are developed using hydraulic models that cannot accurately represent the complex flows in floodplains and urban environments. The most prevalent and widely used flood estimation models solve the Saint Venant or Shallow Water equations in one-dimension (Bates and De Roo 2000). Flood inundation is typically determined by developing cross sections perpendicular to the channel for one-dimensional flow modeling and using either steady or unsteady modeling approaches (Hudock 2006). The area of inundation is subsequently determined by connecting water

surface elevations at each cross section and determining the flood area by interpolation (Bates and De Roo 2000). Although this method does a good job of hydraulically routing the flood wave for truly one-dimensional flows, these models cannot accurately represent the complex flows present in floodplains and urban environments (Bousmar et al. 2004). Despite efforts to represent two-dimensional flow with one-dimensional methods (Ervine and MacCleod 1999; Willems et al. 2002), it is recommended that higher-order models, such as two-dimensional models, be used for flood inundation modeling (Knight and Shiono 1996; Bates et al. 1998; NRC 2009).

Two-dimensional models are becoming more widely used (Beffa and Connell 2001; Bradford and Sanders 2002; Lin et al. 2003, Zhou et al. 2004) since these models have significantly greater ability to determine flow velocity and direction, and thus inundation area when compared to one-dimensional models (TRB 2006). Additionally, using 2D models eliminates the need for a secondary process, such as a DEM subtraction from a water surface, to map flood inundation (Bates and De Roo 2000). However, without making simplifications to the governing equations, solution of the shallow water equations can be difficult due to the presence of numerical oscillations near discontinuities, such as near the wetting/drying front (Toro 2001). Recent success in preventing spurious oscillations has been through the use of finite volume schemes (Beffa and Connell 2001; Bradford and Sanders 2002; Lin et al. 2003; Zhou et al. 2004) and finite difference methods (Fennema and Chaudhry 1990; Jin and Fread 1997; Tinsanchali and Rattanapitikon 1999) that are total variation diminishing (TVD). One of the most widely used methods that is TVD is the monotone upstream-centered scheme for conservation laws (MUSCL) (Mignot et al. 2006; Liao et al. 2007).

The major limitation of two-dimensional models is that they are computationally demanding and require considerable expertise to execute when using complex numerical schemes (NRC 2009). Compounding the computational cost, many of the already complex numerical models use a predictor-corrector approach to achieve accuracy (Fennema and Chaudhry 1990; Tingsanchali and Rattanapitikon 1999; Beffa and Connel 2001; Bradford and Sanders 2002; Lin et al. 2003; Liao et al 2007). This computational cost limits the ability of two-dimensional models to be used in fast-response flood analyses.

To decrease computational cost, some models make simplification to the governing equations (Bates and De Roo 2000; Bradbrook et al. 2004; Chen et al. 2005) through the elimination of the inertial terms. While these raster-based and diffusion wave models have advantages in terms of their ease of formulation and computational efficiency, questions remain over their relatively simple representation of complex flow processes due to the lack of representation of momentum transfer in complex regions such as floodplains and urban environments (Yu and Lane 2006).

Flood modeling and simulation can greatly facilitate decision makers in flood events provided these capabilities can be accomplished rapidly and accurately. The National Infrastructure Simulation and Analysis Center (NISAC) is a recognized source of expertise on issues germane to critical infrastructure protection, preparedness, and continuity of operations. NISAC draws on the modeling, simulation, and analysis expertise at Los Alamos and Sandia National Laboratories to systematically quantify the potential consequences of damage to critical infrastructure from natural and manmade disasters. These analyses help decision makers understand infrastructure protection,

mitigation, response, and recovery options. They also help decision makers prepare for and respond to the physical, economic, and security implications to our nation if these infrastructures are disrupted. Due to the nature of some events, modeling and simulation results and consequence assessment must be completed within a time frame of hours to days. In 2008, the NISAC Fast-Response Team provided more than 80 as-needed analysis products, including quick assessment and evaluation of impacts due to flooding in the Midwest and Hurricanes Gustav, Ike, and Holly.

To meet the objectives of fast-response flood modeling and simulation and overcome the computational expense limitations of two-dimensional flood modeling, a two-dimensional model has been developed using the complete shallow water equations while using a simple, yet accurate upwind finite difference method. The model has been validated with both laboratory and real-world case studies and shows great accuracy, even when compared to more complex two-dimensional models. The numerical model and validation studies are presented in the following sections.

2.2 Methodology

2.2.1 Governing Equations

The shallow water equations are developed from the Navier-Stokes equations by integrating the horizontal momentum and continuity equations over the depth. Thus, the shallow water equations are often referred to as the depth-averaged or depth-integrated shallow water equations. Vreugdenhil (1994), Toro (2001), and Leveque (2002) provide

details on derivation of the equations. The non-conservative form of the equations are shown in Equations 2.1, 2.2, and 2.3, which consist of a continuity equation and momentum in the x and y direction, respectively.

$$\frac{\partial h}{\partial t}+\frac{\partial uh}{\partial x}+\frac{\partial vh}{\partial y}=0 \tag{2.1}$$

$$\frac{\partial u}{\partial t}+u\frac{\partial u}{\partial x}+v\frac{\partial u}{\partial y}+g\frac{\partial H}{\partial x}+gS_{fx}=0 \tag{2.2}$$

$$\frac{\partial v}{\partial t}+u\frac{\partial v}{\partial x}+v\frac{\partial v}{\partial y}+g\frac{\partial H}{\partial y}+gS_{fy}=0 \tag{2.3}$$

where h is the water depth, H is the water surface elevation, u is the velocity in the x-direction, v is the velocity in the y-direction, t is time, g is the gravitational constant, S_{fx} is the friction slope in the x-direction, and S_{fy} is the friction slope in the y-direction. The friction slope terms are estimated based on the Manning formula.

The shallow water equations are non-linear hyperbolic partial differential equations, which tend to admit discontinuous solutions; therefore, numerical schemes that are TVD must be used. Perhaps the simplest method which is TVD and will never yield oscillatory solutions is a first-order upwind method, where stability is achieved through numerical diffusion (Patankar 1980; Ferziger and Peric 2002). The upwind differencing scheme uses a backward or forward differencing approximation for the convective terms in the equations, depending on the direction of the local velocity. The following sections describe the implementation of the shallow water equations in a flood estimation model using an upwind finite differencing scheme.

2.2.2 Spatial Discretization

The principle dataset in two-dimensional flood modeling is topographic data, which is readily available from the United States Geological Survey (USGS) for the United States. Because the grid structure of USGS digital elevation model (DEM) data is structured, this model is developed using a structured grid such that this data can be quickly and simply ingested, eliminating the need for a secondary grid generation tool. There are two methods used for placement of the variables (h,u,v) on a structured grid. The first method, the colocated arrangement, places all variables at the center of the cell. The advantage of this approach is its very straightforward implementation. The disadvantage is that solutions on a colocated grid can give oscillatory solutions, similar to a checkerboard (Vreugdenhil 1994; Ferziger and Peric 2002). The second method, the staggered arrangement, does not place all variables in the same location. Fig. 2.1 shows the variable placement for this numerical model in a staggered arrangement.

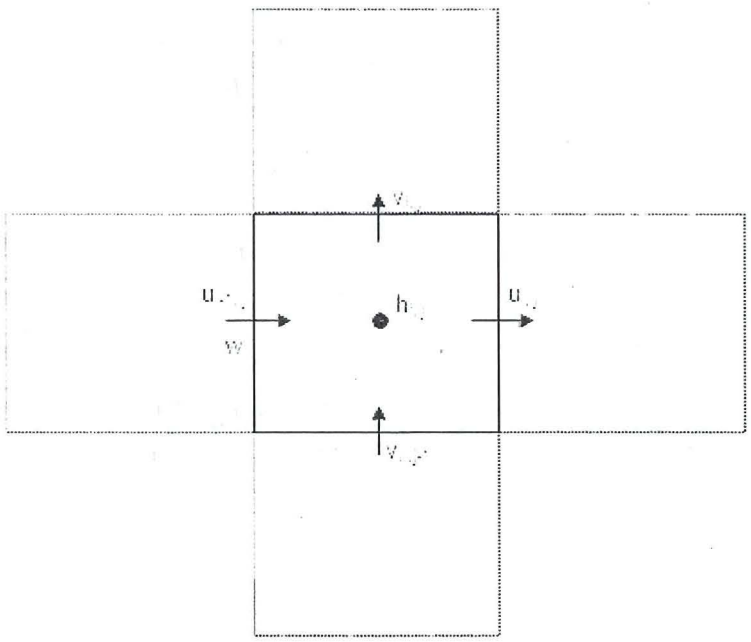

Fig. 2.1. Staggered arrangement of shallow water equation variables.

First, the depth variable, h, is determined through solution of the continuity equation. Rearranging the continuity equation as shown in Equation 2.4, it can now be solved for h.

$$\frac{\partial h}{\partial t} = -\left(\frac{\partial uh}{\partial x} + \frac{\partial vh}{\partial y}\right) \tag{2.4}$$

The discretization of the convective terms in the continuity equation is slightly different than most upwind finite difference approaches. Because the velocity vectors are already located at the faces of the control volume, there is no need to interpolate them to the cell center; rather the fluxes can be computed from these faces. Equations 2.5 and 2.6 show the discretized form of the convective terms.

$$\frac{\partial uh}{\partial x} = \frac{u_{i,j}h_E - u_{i-1,j}h_W}{dx} \tag{2.5}$$

$$\frac{\partial vh}{\partial y} = \frac{v_{i,j}h_N - v_{i,j-1}h_S}{dy} \tag{2.6}$$

where

$$h_E = \begin{cases} h_{i,j} & \text{if } u_{i,j} > 0 \\ h_{i+1,j} & \text{if } u_{i,j} < 0 \end{cases} \tag{2.7}$$

$$h_W = \begin{cases} h_{i-1,j} \text{ if } u_{i-1,j} > 0 \\ h_{i,j} \text{ if } u_{i-1,j} < 0 \end{cases} \tag{2.8}$$

$$h_N = \begin{cases} h_{i,j} \text{ if } v_{i,j} > 0 \\ h_{i,j+1} \text{ if } v_{i,j} < 0 \end{cases} \tag{2.9}$$

$$h_S = \begin{cases} h_{i,j-1} \text{ if } v_{i,j-1} > 0 \\ h_{i,j} \text{ if } v_{i,j-1} < 0 \end{cases} \tag{2.10}$$

In this case the variable h is taken from the direction from the local velocity.

The momentum equation discretization follows a more traditional upwind finite difference approach. The momentum in the x direction is shown in Equation 2.11.

$$\frac{\partial u}{\partial t} = -\left(u_{i,j} \frac{\partial u}{\partial x} + \overline{v}_{i,j} \frac{\partial u}{\partial y} + g \frac{\partial H}{\partial x} + gSfx_{i,j} \right) \tag{2.11}$$

The convective terms in the equation are discretized using either a forward difference or backward difference, depending on the direction of the local velocity, as shown in Equations 2.12 and 2.13.

$$\frac{\partial u}{\partial x} = \begin{cases} \dfrac{u_{i,j} - u_{i-1,j}}{dx}, u_{i,j} > 0 \\ \dfrac{u_{i+1,j} - u_{i,j}}{dx}, u_{i,j} < 0 \end{cases} \tag{2.12}$$

$$\frac{\partial u}{\partial y} = \begin{cases} \dfrac{u_{i,j} - u_{i,j-1}}{dy}, \bar{v}_{i,j} > 0 \\ \dfrac{u_{i,j+1} - u_{i,j}}{dy}, \bar{v}_{i,j} < 0 \end{cases} \tag{2.13}$$

Where $\bar{v}_{i,j}$ is the local velocity in the y direction, taken from the average of the surrounding cells as shown in Equation 2.14.

$$\bar{v}_{i,j} = \frac{v_{i,j} + v_{i+1,j} + v_{i,j-1} + v_{i+1,j-1}}{4} \tag{2.14}$$

The non-convective term representing the water surface gradient can be discretized using a second-order accurate central difference scheme, as shown in Equation 2.15.

$$\frac{\partial H}{\partial x} = \frac{H_{i+1,j} - H_{i,j}}{dx} \tag{2.15}$$

The friction term, S_{fx}, is represented using Manning's equation, as shown in Equation 2.16

$$Sfx_{i,j} = \frac{\bar{n}_{xi,j}^{\,2} u_{i,j} \sqrt{u_{i,j}^2 + \bar{v}_{i,j}^2}}{\left(\overline{hx} + h_{extra}\right)^{\frac{4}{3}}} \tag{2.16}$$

where h_{extra} is a small amount of water added to prevent the friction slope from being overestimated as the depth of water, h, approaches zero; n_x and h_x are the average

roughness and depth, respectively, at the location of the velocity vector, u, as shown in Equations 2.17 and 2.18 below.

$$\overline{n}_{xi,j} = \frac{n_{i,j} + n_{i+1,j}}{2} \tag{2.17}$$

$$\overline{hx} = \frac{h_{i,j} + h_{i+1,j}}{2} \tag{2.18}$$

The discretization of the momentum in the y direction follows the same approach as the discretization for the momentum in the x direction. First, the momentum equation is arranged such that the velocity, v, may be solved, as shown in Equation 2.19.

$$\frac{\partial v}{\partial t} = -\left(\overline{u}_{i,j} \frac{\partial v}{\partial x} + v_{i,j} \frac{\partial v}{\partial y} + g \frac{\partial H}{\partial y} + gSfy_{i,j} \right) \tag{2.19}$$

The convective terms are evaluated at the location of the velocity vector, v, using the upwind differencing scheme, as shown in Equations 2.20 and 2.21.

$$\frac{\partial v}{\partial x} = \begin{cases} \dfrac{v_{i,j} - v_{i-1,j}}{dx}, \overline{u}_{i,j} > 0 \\ \dfrac{v_{i+1,j} - v_{i,j}}{dx}, \overline{u}_{i,j} < 0 \end{cases} \tag{2.20}$$

$$\frac{\partial v}{\partial y} = \begin{cases} \dfrac{v_{i,j} - v_{i,j-1}}{dx}, v_{i,j} > 0 \\ \dfrac{v_{i,j+1} - v_{i,j}}{dx}, v_{i,j} < 0 \end{cases} \tag{2.21}$$

where $\overline{u}_{i,j}$ is the average velocity in the x direction at the location of the velocity in the y direction, as shown in Equation 2.22.

$$\overline{u}_{i,j} = \frac{u_{i,j} + u_{i,j+1} + u_{i-1,j} + u_{i-1,j+1}}{4} \tag{2.22}$$

Again, the non-convective term representing the water surface gradient in the y direction is discretized using a second-order accurate central difference scheme, as shown in Equation 2.23.

$$\frac{\partial H}{\partial y} = \frac{H_{i,j+1} - H_{i,j-1}}{dx} \tag{2.23}$$

The representation of the friction slope is the same as in the x direction as shown in Equation 2.24.

$$Sfy_{i,j} = \frac{\overline{n}_{y_{i,j}}^{\,2} v_{i,j} \sqrt{v_{i,j}^2 + \overline{u}_{i,j}^2}}{\left(\overline{hy} + h_{extra}\right)^{\frac{4}{3}}} \tag{2.24}$$

where n_y and h_y are the average roughness and depth at the cell location of the velocity in the y direction, respectively, as shown in Equations 2.25 and 2.26.

$$\overline{n}_{y_{i,j}} = \frac{n_{i,j} + n_{i,j+1}}{2} \tag{2.25}$$

$$\overline{hy} = \frac{h_{i,j} + h_{i,j+1}}{2} \tag{2.26}$$

2.2.3 Time Discretization

An implicit discretization of the shallow water equations involves the simultaneous solution of a large number of nonlinear equations. Additionally, the time

step in these methods cannot be arbitrarily large, making this method impractical (Casulli 1989). Therefore, this model uses an explicit Euler time integration method. The time discretized form of the continuity and momentum equation are shown in Equations 2.27, 2.28, and 2.29.

$$h_{i,j}^{t+1} = h_{i,j}^{t} - \left(\frac{\partial uh}{\partial x} + \frac{\partial vh}{\partial y} \right)_{i,j}^{t} \tag{2.27}$$

$$u_{i,j}^{t+1} = u_{i,j}^{t} - \left(u_{i,j} \frac{\partial u}{\partial x} + \bar{v}_{i,j} \frac{\partial u}{\partial y} + g \frac{\partial H}{\partial x} + gSfx_{i,j} \right)_{i,j}^{t} \tag{2.28}$$

$$v_{i,j}^{t+1} = v_{i,j}^{t} - \left(\bar{u}_{i,j} \frac{\partial v}{\partial x} + v_{i,j} \frac{\partial v}{\partial y} + g \frac{\partial H}{\partial y} + gSfy_{i,j} \right)_{i,j}^{t} \tag{2.29}$$

where t_{+1} is the time at which the variables are currently being calculated, and t is time at which the variables are previously known.

This method is subject to the stability restriction imposed by the Courant-Friedrich condition. Therefore, the time step in this model is limited as shown in Equation 2.30.

$$\Delta t < C \frac{dn}{v \max} \tag{2.30}$$

where C is the Courant number and must be less than unity, dn is the smallest spatial dimension for a cell in the x or y direction, and $vmax$ is the maximum velocity.

2.2.4 Model Implementation

The above equations were used to develop a fast-response flood estimation model implemented within Java. Java has many benefits, such as its object orientation semantics and cross-platform portability (Moreira et al. 2000), but perhaps the biggest advantage is the ability of Java to be included in service oriented architectures (SOA) and web-enabled products such that it can effectively be used in decision analysis tools, facilitating rapid synthesis of results and consequence assessment. The model architecture is shown in Fig. 2.2 below.

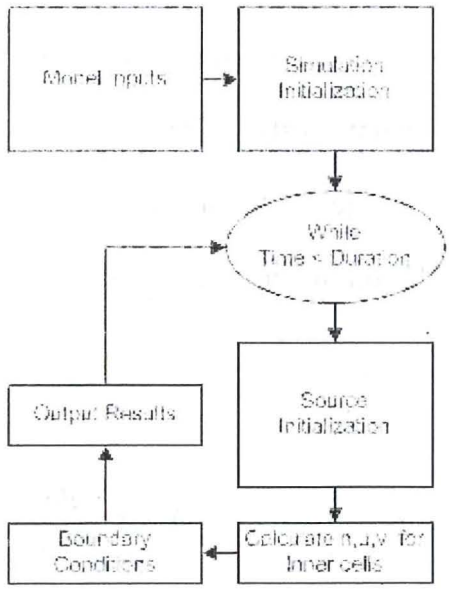

Fig. 2.2. Flood model flow chart.

2.3 Model Validation

The ability of the model to accurately estimate flood inundation is illustrated through three validation studies. The validation studies include comparisons to laboratory controlled experiments, as well as a real-world flood inundation event to show the models ability to estimate flood velocities and depths over irregular topography. The first study is a simulation of a physical experiment conducted by the Waterways Experiment Station (WES), with a comparison of results to both the measured depths and velocities as well as published results from a two-dimensional, second-order accurate model. The second study compares simulation results to measured results gathered from a laboratory physical model to show the models ability to represent unsteady conditions, such as reflected waves. Finally, the model is used to simulate the Taum Sauk dam failure and is compared to published high water mark data.

2.3.1 WES Experiment

Laboratory physical experiments were conducted at the Waterways Experiment Station and depths and velocities were collected at various locations in the physical model (WES 1960). The physical model consisted of a 122 m and 1.22 m wide channel with a constant bed slope of .005 and a bed roughness of .009. The channel consisted of a dam located 61 m from the downstream end and at an elevation of 0.305 m with a slot

width of 0.122 m in the center of the channel. The dam height was 0.61 m, as was the water surface elevation upstream of the dam.

A numerical model of the WES physical model was setup using a constant cell size of 0.061 m. The velocity perpendicular to walls was set equal to zero, and the outlet was modeled using a non-reflective boundary condition. The simulation results were compared to the measured data collected, as well as modeled results taken from Bradford and Sanders (2002) in which a two-dimensional finite volume method using Roes's approximate Riemann solver was used to compute the fluxes and the MUSCL scheme and predictor-corrector time stepping is used to develop a second-order accurate solution.

The results are compared at 76.25 m, 53.375 m, and 15.25 m from the downstream end and are shown in Fig. 2.3-2.5, respectively.

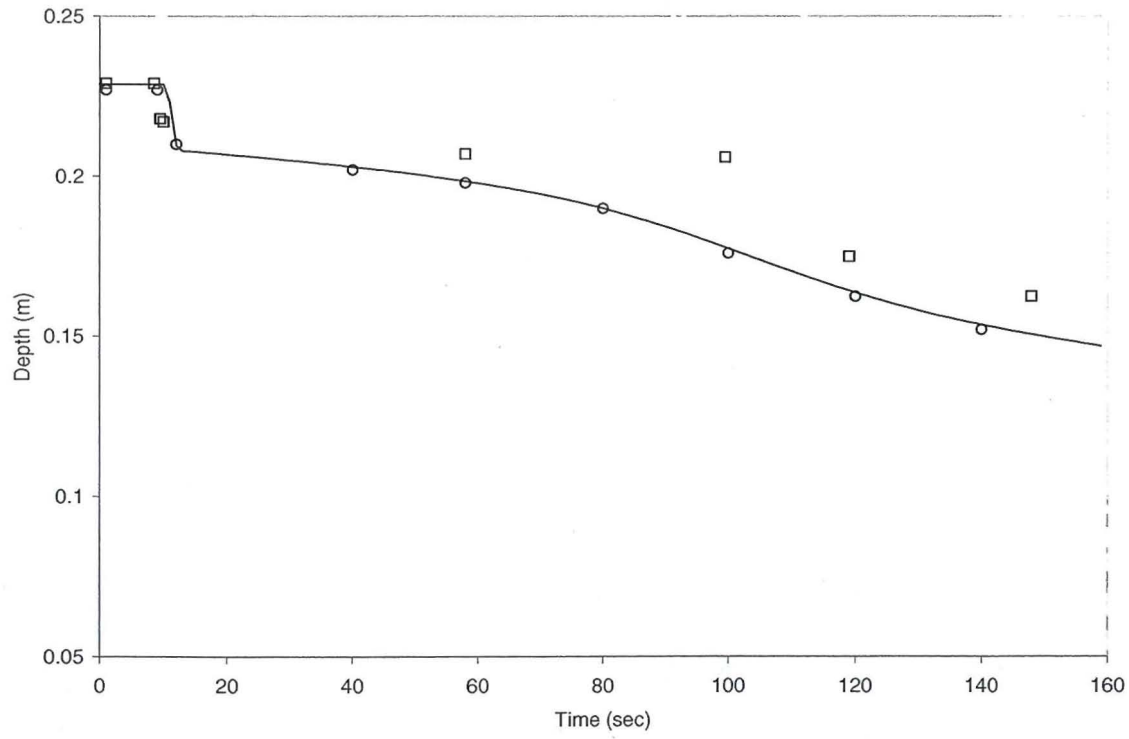

Fig. 2.3. Simulated depths at 76.25 m from downstream end compared to WES (squares) and Bradford and Sanders (2002) (circles).

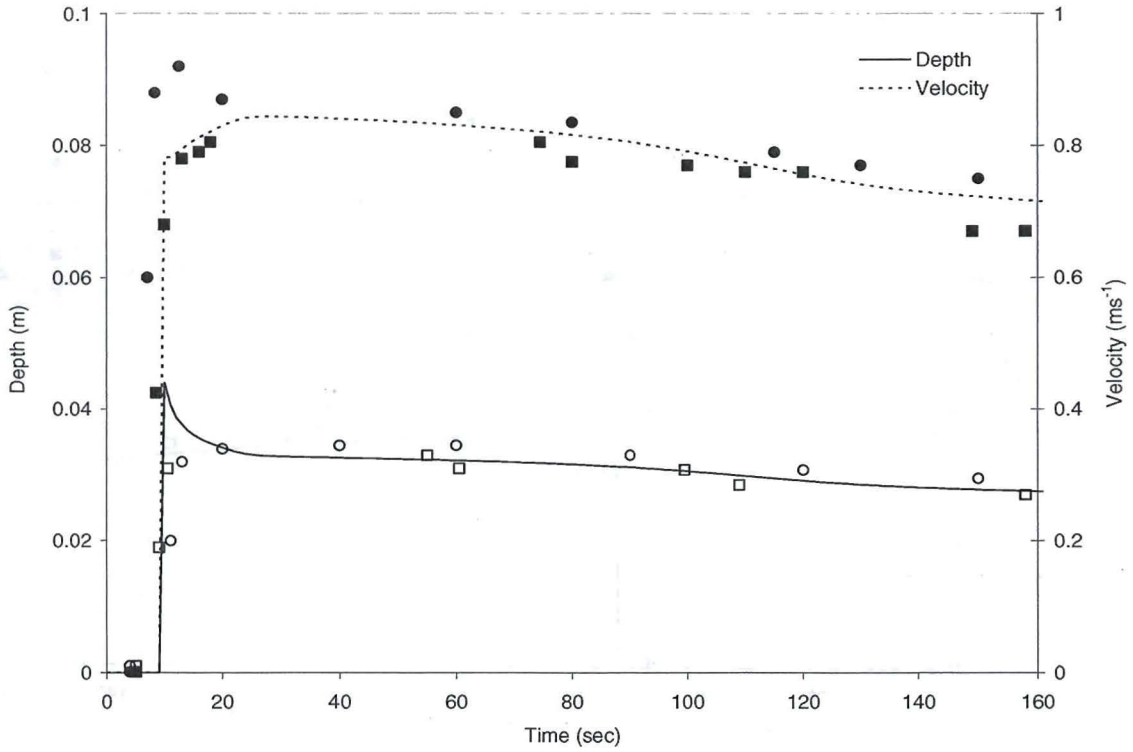

Fig. 2.4. Simulated depths and velocities at 53.375 m from downstream end compared to WES (squares) and Bradford and Sanders (2002) (circles).

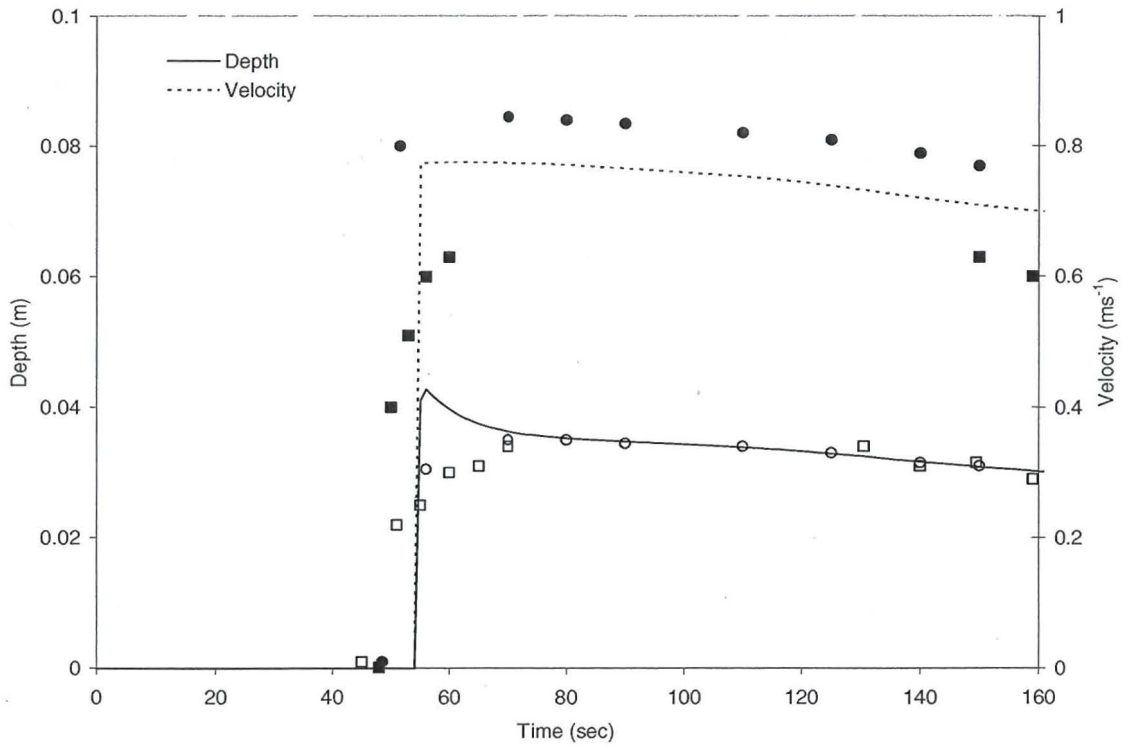

Fig. 2.5. Simulated depths and velocities at 15.25 m from downstream end compared to WES (squares) and Bradford and Sanders (2002)(circles).

Overall, the simulation results compare well with both the measured data and the model developed by Bradford and Sanders (2002). The simulated depth upstream of the dam (Fig. 4.3) shows that the arrival of the depression wave was accurately modeled, though underpredicted depths later in the simulation. Just downstream of the dam breach (Fig. 4.4) simulated depths and velocities compared well throughout the entire simulation. In fact, the velocities estimated at this point (taken as the average across the length of the channel (Bradford and Sanders 2002)) agreed better with the measured data than the second-order accurate model. Near the outlet (Fig. 4.5) the depths were in good agreement with both the measured results and the second-order accurate model, though

the arrival of the flood wave was slightly late. The velocities at this location were significantly overestimated. Bradford and Sanders (2002) reason that the measured velocity was underestimated. The velocity was estimated by timing the movement of particles at the surface of the water, and then multiplying this velocity by the depth average velocity (0.8) determined under steady, uniform flow conditions. Because the flow in this simulation is not uniform or steady, the depth average velocity is likely closer to 1.0, and therefore, the estimated velocity is underestimated.

2.3.2 Laboratory Controlled Physical Model

A physical dam break model was built in a laboratory, similar to the model described by Tinsanchali and Rattanapitikon (1999). The model consists of a reservoir and a floodplain, separated by a wall with a 0.1 m slot at the centerline. A 0.5 m outlet is located at the end of the floodplain. Plywood was used to construct the reservoir and floodplain surfaces. Fig. 2.6 and 2.7 show a plan and profile view of the physical model.

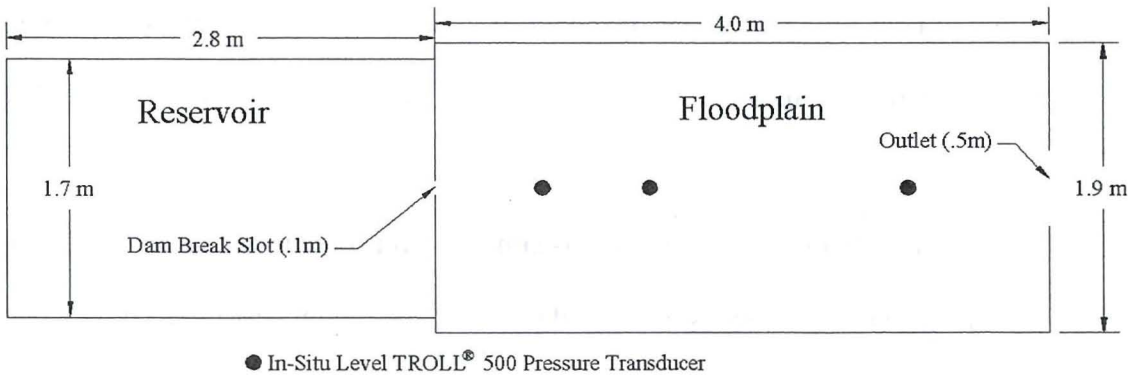

Fig. 2.6. Plan view of laboratory physical model

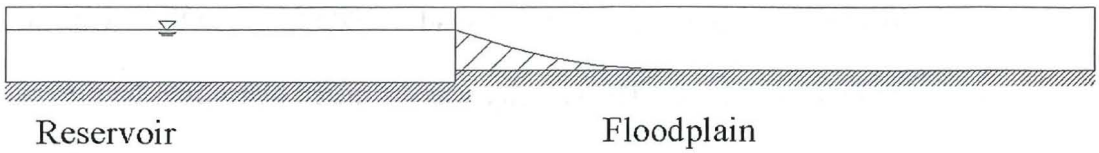

Fig. 2.7. Profile view of laboratory physical model

A gate controls the slot between the reservoir and the floodplain. The near instantaneous lifting of the gate and the immediate uncontrolled release of water from the reservoir simulates the dam break. The outflow from the reservoir is measured by the change in storage in the reservoir.

The water depths in the floodplain are measured using three In-Situ Level TROLL 500 pressure transducers, placed at distances of 0.7 m, 1.4 m, and 3.1 m from the reservoir along the centerline. In an effort to reduce the effect of measuring the depth on the flood wave, the sensors were placed underneath the floodplain. The manufacturer-expected accuracy of the sensors is ± .05% of maximum range (3.5 m). The sensor accuracy was tested in a controlled laboratory exercise and it was found that, in order to increase the accuracy for the range of depths expected in this experiment, a minimum depth of near 2 cm on the sensor should be maintained. To accomplish this, the sensors were lowered ~2 cm below the floodplain then filled with water to the level of the floodplain.

The laboratory dam break was simulated for three initial heads: 25 cm, 15 cm, and 10 cm. The range of heads were used to determine model performance with over a wide range of flows. Each initial head was simulated several times to give an indication as to the consistency of the experiment and provide a range of expected values for each sensor.

From the laboratory exercise, it is observed that the flow releases from the reservoir and spreads out two-dimensionally over the floodplain and is in the supercritical flow regime for a distance from the gate. Some flow comes in contact with the side walls and is reflected back toward the center, forming a hydraulic jump. As the flow reaches the end of the floodplain, some flow leaves via the 0.5 m outlet, while the remaining flow is reflected back upstream and stalls near the second sensor. The speed at which the wave moves and the depths that are obtained range based on the initial reservoir head.

Numerical representation of the physical model was completed by creating a mesh at 0.02 m resolution consisting of approximately 36,000 cells. Consideration of boundary conditions included walls and a free outlet. The walls were represented numerically by forcing no-slip boundary conditions, while the free outlet boundary condition was governed by the minimum of critical and normal depth.

Because the roughness of the plywood was not known prior to simulation, multiple simulations were completed for each head using a range of constant roughness values. From the simulations, it was found that a roughness value of 0.0115 yielded the most similar results to the measured data, which is similar to published data (Sturm 2001). Fig. 2.8 below shows a snapshot of the 25 cm initial head simulation. The figure shows the area of supercritical region directly downstream of the breach, as well as the traveling reflected wave near the outlet.

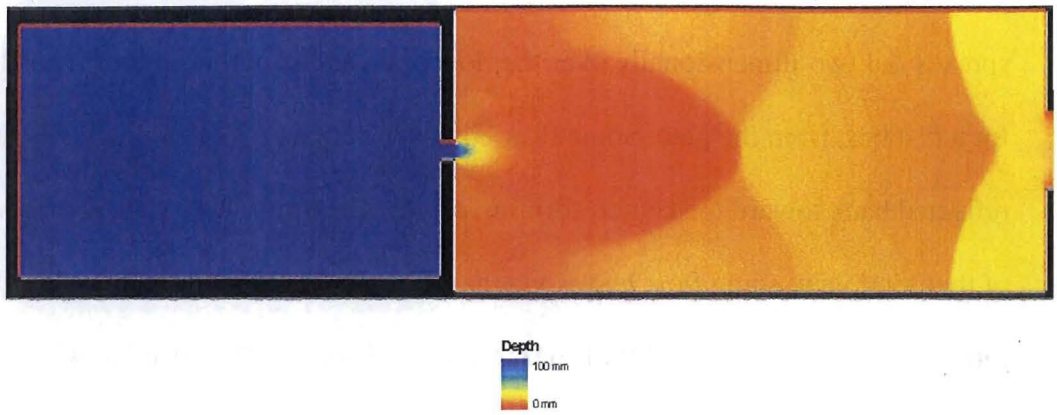

Fig. 2.8. Simulation of 25 cm initial head at $t = 9.25$ sec.

In general, the depths measured by the sensors compared well with the simulated depths. Fig. 2.9-2.11 below shows the measured depths for the sensors (error bars representing the range of values, maximum and minimum, obtained from the laboratory model) and the simulated depths for an initial head of 25 cm.

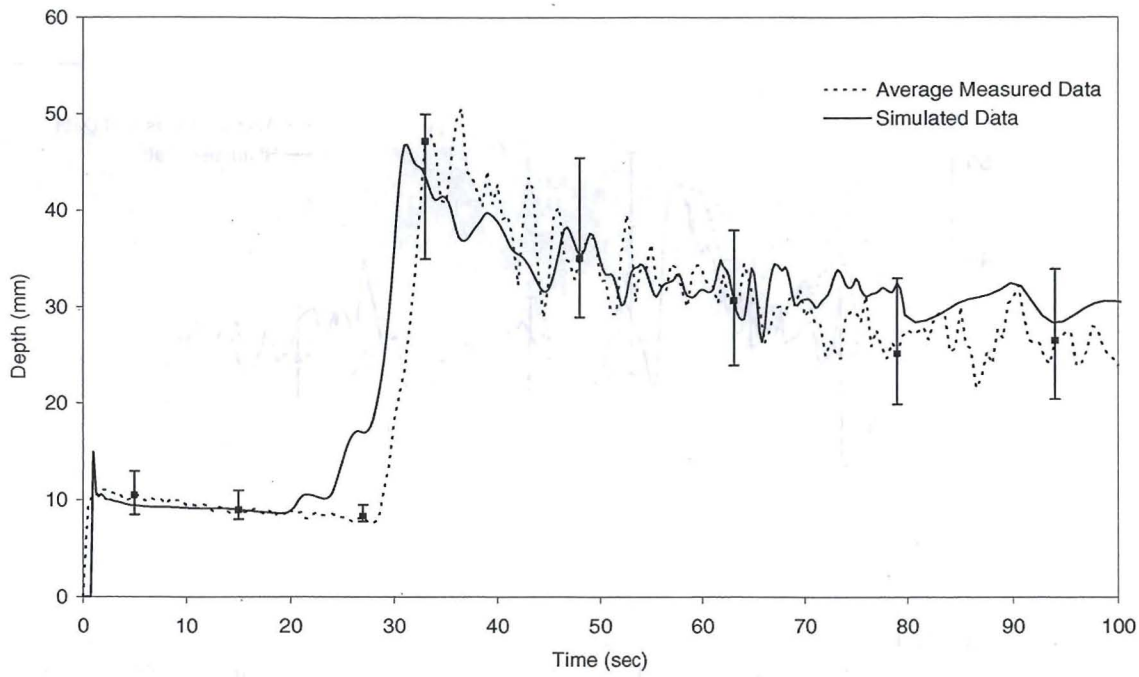

Fig. 2.9. Head measurement at sensor 1 for initial head of 25cm.

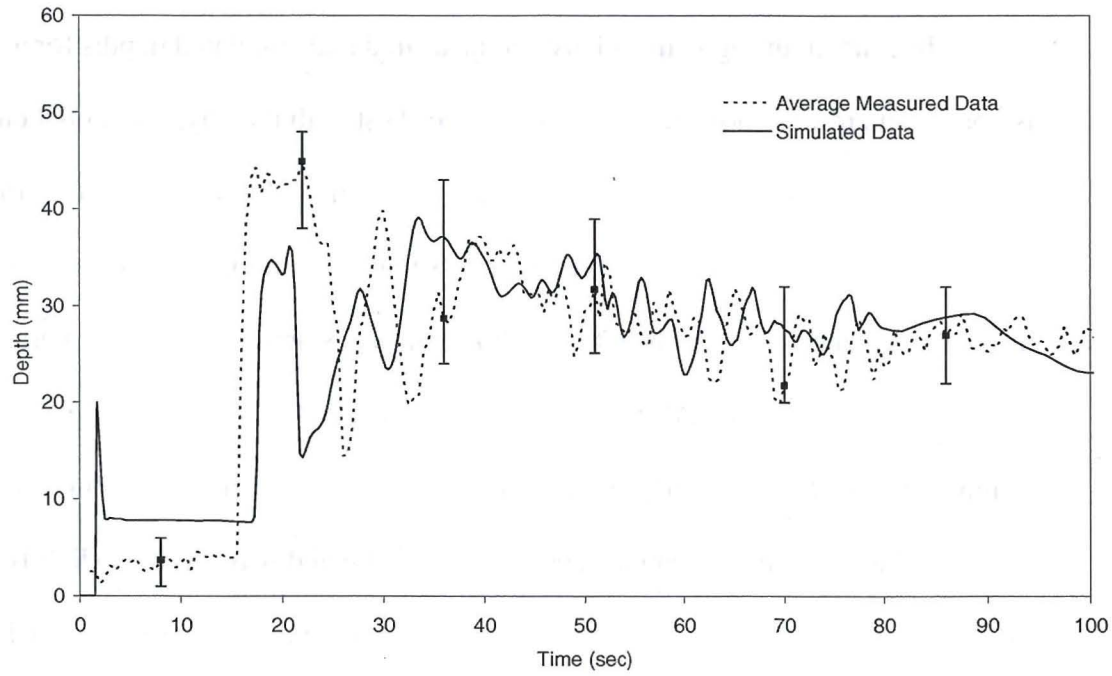

Fig. 2.10. Head measurement at sensor 2 for initial head of 25cm.

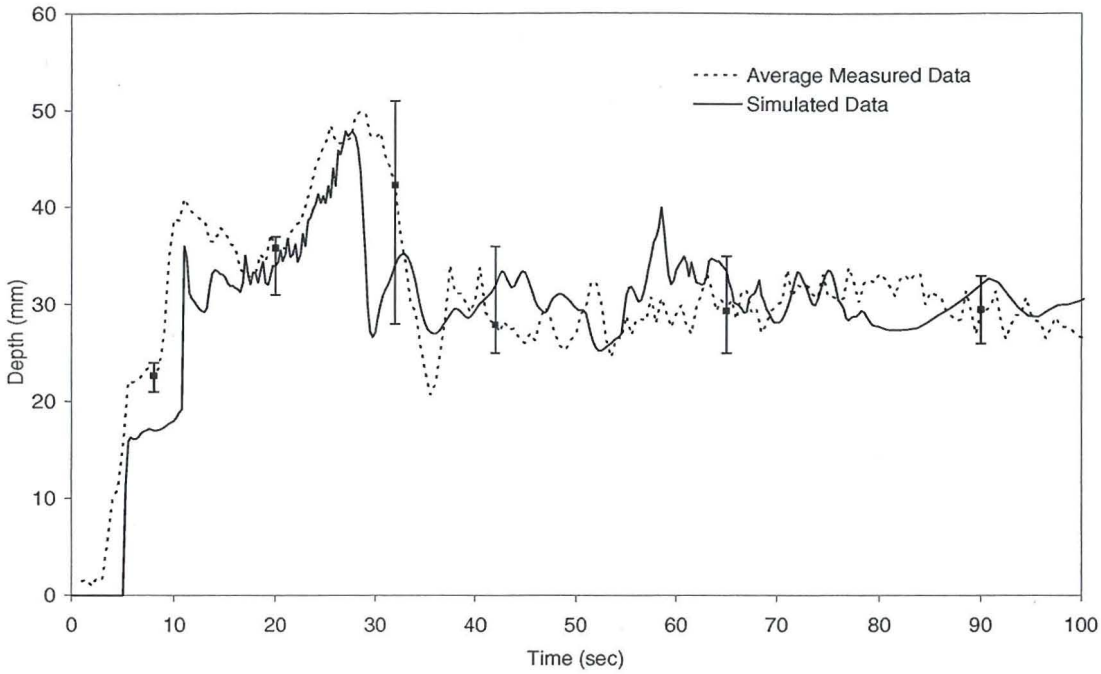

Fig. 2.11. Head measurement at sensor 3 for initial head of 25cm.

In general, the agreement between measured and simulated depths for all sensors is good. The results show that the model agrees best with the physical model once the reflected waves dampen and the water begins to stabilize. In most cases, the simulated peak depths from the reflected waves were less than measured, which is expected for an upwind difference scheme since this method achieves stability through numerical diffusion. The measured and simulated results at sensor 1 had the best agreement. The initial wave depth was slightly high, but was within the measured range until the reflected wave reached the sensor location. The simulated reflected wave arrived slightly earlier than the measured wave, but afterwards remained within the range of measured values.

Sensor 2 had the largest difference between simulated and measured depths, though in general the results are acceptable. As stated previously, the observed location

of the hydraulic jump is near this sensor. Simulations showed that the exact location of the hydraulic jump was sensitive to roughness values selected, and therefore, significantly different depths could be measured. The initial depth is slightly higher than the range of measured values, and the reflected wave is slightly lower than the range of measured values, but again remains within the range of measured values for the remainder of the simulation.

Sensor 3 also shows good agreement. The initial wave arrives slightly later than the measured wave, and the simulated reflected wave depth is again lower than measured depth. Once again, when the reflected wave passes, the simulated depths are within the range of measured depths. Comparison of the other initial heads resulted in similar results.

The results of this validation exercise show that the model has the ability to predict the timing and depths of the floodwave resulting from the sudden release of water. This study also showed the models ability to simulate highly unsteady flow conditions, as represented by the presence of both supercritical and subcritical flow, hydraulic jumps, and reflected waves from walls, even though the simulated peak depths from the resulting reflected waves were generally underestimated by the model.

2.2.3 Taum Sauk Dam Breach

Validation data from actual flood events are rare. While validation studies from laboratory experiments provide valuable information in terms of model performance, they cannot represent real-world environments with irregular topography and features.

This section describes a unique opportunity to compare model simulations of a dam breach to a real-world dam breach.

Taum Sauk is a pump-storage hydroelectric power plant located in Reynolds County, Missouri, with a storage capacity of near 5.7 million cubic meters. The reservoir sits approximately 232 m above the floodplain of the East Fork Black River. On December 14, 2005, a 207 m wide section of the reservoir failed suddenly as a result of overfilling of the storage facility and emptied within 25 minutes. The resulting flood wave rushed down Proffit Mountain and into Johnson's Shut-Ins State Park, and subsequently into the East Fork Black River and finally into a lower storage reservoir. Within hours after the failure, field crews began collecting high water marks resulting from the flood (USGS, 2006). While high water mark data does not provide any indication on flood timing, or even the depths of water spatially, they do provide the ability to determine the models ability to estimate the flood extent which was not shown in the previous validation studies.

The topography for this study was obtained from a USGS 10 m DEM covering the extent of the flood event. A hydrograph was obtained from a USGS flood analysis of the event (USGS, 2006), in which the discharge was developed from a volume analysis of the embankment failure. The peak discharge in this study was determined to be ~8,100 cubic meters per second (cms), peaking approximately six minutes after the breach. Because the breach discharge was not explicitly measured, it is noted that the uncertainty of the discharge hydrograph could potentially add to the uncertainty in model estimates. The estimated discharge hydrograph is shown in Fig. 2.12 below.

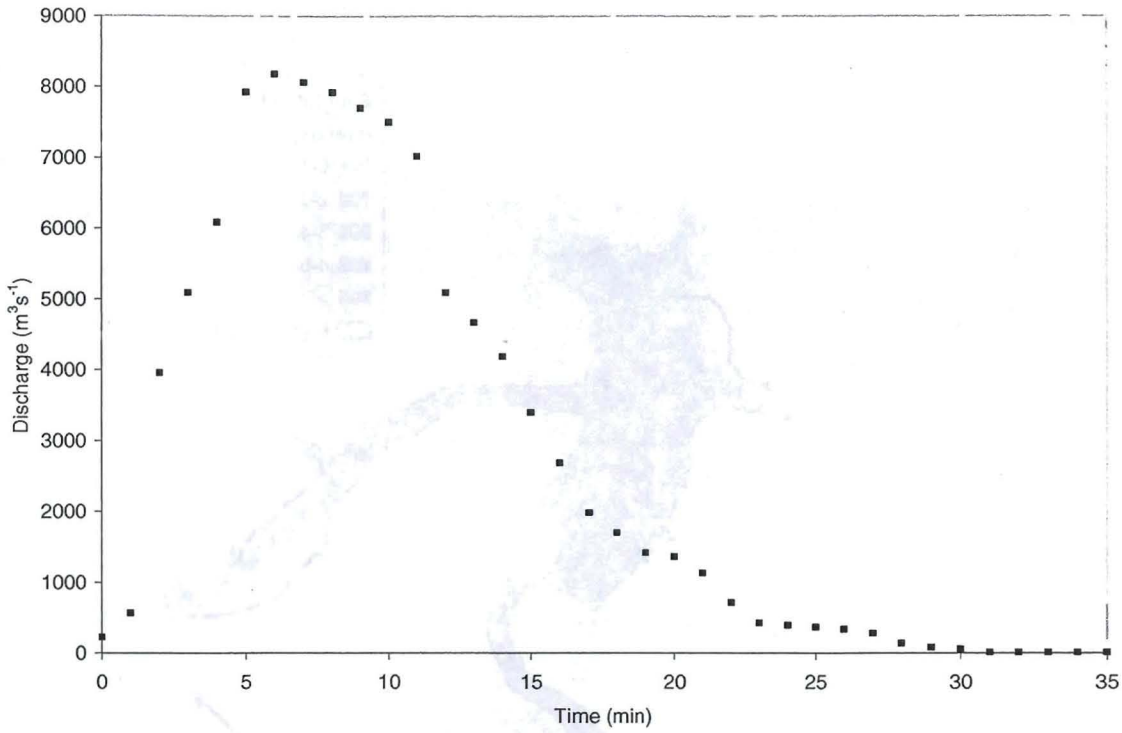

Fig. 2.12. Taum Sauk breach hydrograph (from USGS 2006).

Under flood conditions (e.g. dam break), areas inundated are not typical of floodplain areas, and distributed roughness values are not typically known. Therefore, it is common practice to use a constant roughness value to represent the roughness over the entire flooded area (Lia et al. 2007; Begnudelli and Sanders 2007). Through as series of simulations, it was determined that a roughness of 0.035 represented the Taum Sauk failure closest. Fig. 2.13 shows the simulated flood peak (taken as the maximum value obtained at any location at any time) along with the high water mark data. Note that the comparison between the high water mark and simulated data is limited in this study to locations upstream of the lower reservoir. This is due to the lack of data to accurately model the lower reservoir water levels, as well as the inability of the DEM to represent the downstream control structures.

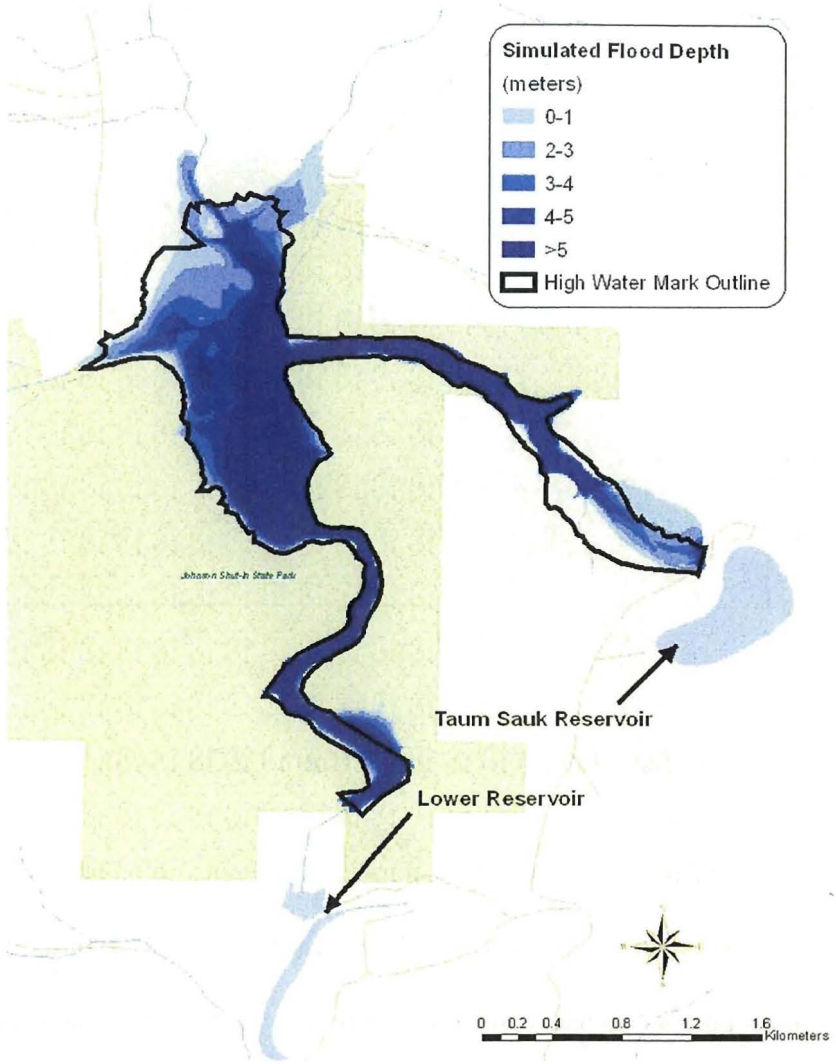

Fig. 2.13. Taum Sauk simulated and observed flooded area.

As Figure 2.11 shows, the simulated results compare well with the measured high water mark data, with an exception near the formation of the breach. This location experienced extensive erosion, or sediment transport, resulting in changes in the local topography. This model does not include sediment transport, thus it does not simulate the change in channel location.

Two metrics are used to determine how well the simulated data fits the high water mark data. First a measure of fit, shown in Equation 2.35, is used to give an overall assessment on how the two datasets relate.

$$Fit = 1 - \frac{A(S_{\text{mod}} \cap S_{obs})}{A(S_{\text{mod}} \cup S_{obs})}(100) \tag{2.35}$$

where S_{mod} and S_{obs} are the inundation extents of the modeled and observed data, respectively. While Equation 2.35 gives an indication of the overall difference between the two datasets, it does not indicate any overestimation or underestimation. To accomplish this, a second metric is used. A statistical comparison between the two datasets can be made by rasterizing the two datasets with a cell size equal to the DEM and creating an error matrix. The error matrix consists of a comparison of flooded areas, assigned a value of 1, and non-flooded areas, assigned a value of 0. Using the error matrix shown in Table 2.1, errors of commission (overestimation) and errors of omission (underestimation) may be calculated, as shown in Equations 2.36 and 2.37 below.

Table 2.1. Taum Sauk flooded area error matrix.

Modeled	Observed	
	0	1
0	109,709	2,006
1	3,782	19,023

$$Commission\ Difference = \left(1 - {}^{P_e}\!/_{P_t}\right)100 \tag{2.36}$$

$$Omission\ Difference = \left(1 - {}^{P_e}\!/_{P_u}\right)100 \tag{2.37}$$

where P_e is the number of common flooded cells, P_t is the total number of modeled wet cells, and P_u is the total number of observed wet cells. Table 2.2 shows the results using both metrics, and Fig. 2.14 visualizes the error matrix results.

Table 2.2 Taum Sauk Flooded Area Statistical Comparison Results

Metric	Percentage
Fit	76.3
Commission Error	16.6

Omission Error	9.5

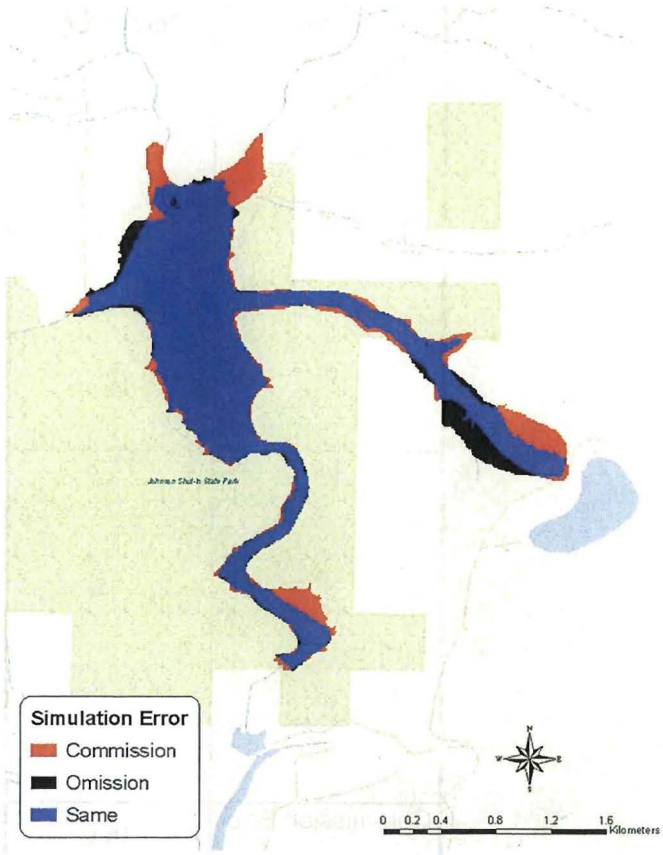

Fig. 2.14. Taum Sauk flooded area error matrix visualization.

As observed previously, the majority of the underestimation is near the formation of the breach. At the same location, there is some overestimation as a result of the

model's inability to represent the sediment transport. The majority of the error located near the state park is an overestimation on the north end. Overall, the model agreed well with the observed high water mark data.

Since the non-conservative and a finite difference formulation of the equations are used, it is important to check the models ability to conserve mass. Unlike the previous two validation studies, this validation study represents a closed system simulation, meaning that all flow entering the system specified by the hydrograph should remain in the system, a check can be made on mass conservation of the numerical model. Mass conservation for the Taum Sauk simulation is shown in Figure 2.13 below.

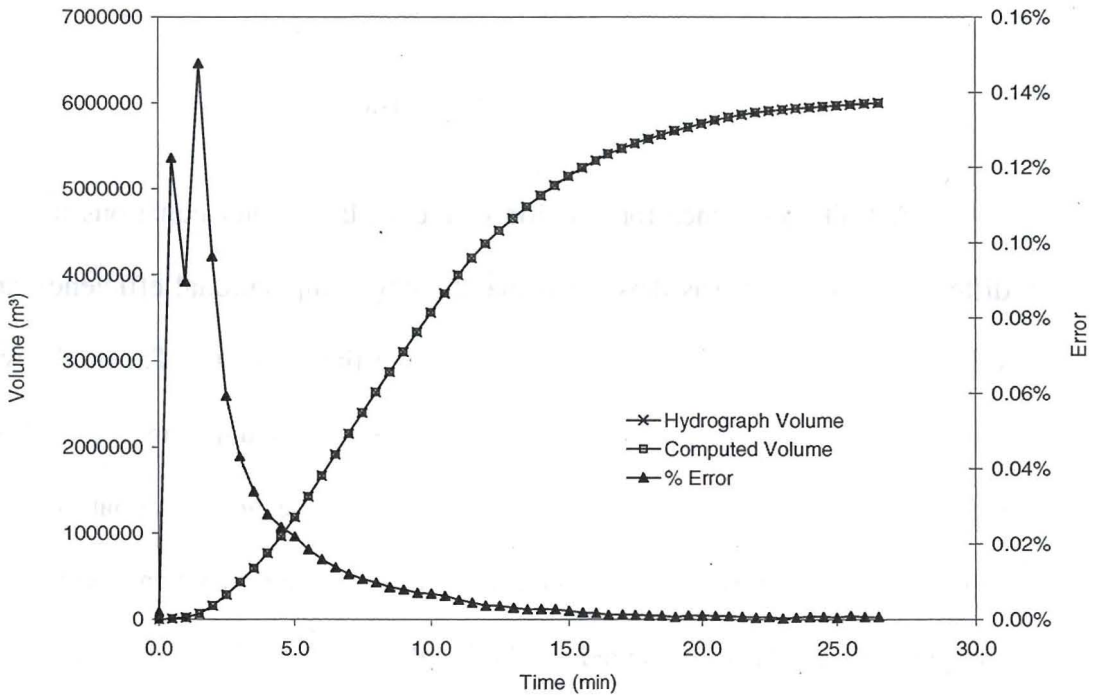

Figure 2.13 Mass conservation check of the Taum Sauk dam breach simulation

The figure shows both the mass that enters the domain specified by the hydrograph and the mass that is computed by the model throughout the simulation. Clearly from the results the numerical model is adequately conserving mass, with a maximum error of .15%.

2.3 Conclusions

A finite difference formulation of the shallow water equations using an upwind differencing method was developed maintaining computational efficiency and accuracy such that it can be used as a fast-response flood estimation tool. The model was validated using both laboratory controlled experiments and an actual dam breach. Through the laboratory experiments, the model was shown to give good estimations of depth and velocity when compared to the measured data, as well as when compared to a more complex two-dimensional model. Additionally, the model was compared to high water mark data obtained from the failure of the Taum Sauk dam. The simulated inundation extent agreed well with the observed extent, with the most notable differences resulting from the inability to model sediment transport. The results of these validation studies

show that a relatively simple numerical scheme used to solve the complete shallow water equations can be used to accurately estimate flood inundation.

Future work will focus on further reducing the computation time needed to provide flood inundation estimates for fast-response analyses. This will be accomplished through the efficient use of multi-core, multi-processor computers coupled with an efficient domain-tracking algorithm, as well as an understanding of the impacts of grid resolution on model results.

2.4 References

Downton, M.W., Miller, J.Z, Pielke, Jr., R.A., 2005. reanalysis of U.S. National Weather Service flood loss database, Natural Hazards Review, February, 13-22.

Pielke, Jr., R.A., M.W. Downton, and J.Z. Barnard Miller, 2002: Flood Damage in the United States, 1926-2000: A Reanalysis of National Weather Service Estimates. Boulder, CO: UCAR.

Pielke, Jr., R.A. and Downton. (2000). Precipitation and Damaging Floods: Trends in the United states, 1932-1997. Journal of Climate, 13(20), 3625-3637.

United Nations Development Programme (UNDP), 2004. A global report: Reducing disaster risk- A challenge for development. John S. Swift Co., USA.

Sturm, T.W., 2001. Open channel hydraulics. McGraw-Hill, Pennsylvania.

Moreira, J.E., Midkiff, S.P., Gupta, M., Artigas, P.V., Snir, M., Lawrence, R.D., 2000. Java programming for high-performance numerical computing. IBM Systems Journal, 39(1), 21-56.

Begnudelli, L, and Sanders, B.F., 2007. Simulation of the St. Francis dam-break flood, Journal of Engineering Mechanics, 133(11), 1200-1212